Article

TRANSPARENT PROCESS OPEN ACCESS

THE EMBO JOURNAL

High-throughput morphometric and transcriptomic profiling uncovers composition of naïve and sensory-deprived cortical cholinergic VIP/CHAT neurons

Nadav Yayon[1,2], Oren Amsalem[1,3], Tamara Zorbaz[1,2,6], Or Yakov[2], Serafima Dubnov[1,2], Katarzyna Winek[1,2], Amir Dudai[1,3], Gil Adam[2], Anna K Schmidtner[1], Marc Tessier-Lavigne[4], Nicolas Renier[5], Naomi Habib[1,3], Idan Segev[1,3], Michael London[1,3] & Hermona Soreq[1,2,*]

Downloaded from https://www.embopress.org on December 26, 2023 from IP 132.64.53.73.

Abstract

Cortical neuronal networks control cognitive output, but their composition and modulation remain elusive. Here, we studied the morphological and transcriptional diversity of cortical cholinergic VIP/ChAT interneurons (VChIs), a sparse population with a largely unknown function. We focused on VChIs from the whole barrel cortex and developed a high-throughput automated reconstruction framework, termed PopRec, to characterize hundreds of VChIs from each mouse in an unbiased manner, while preserving 3D cortical coordinates in multiple cleared mouse brains, accumulating thousands of cells. We identified two fundamentally distinct morphological types of VChIs, bipolar and multipolar that differ in their cortical distribution and general morphological features. Following mild unilateral whisker deprivation on postnatal day seven, we found after three weeks both ipsi- and contralateral dendritic arborization differences and modified cortical depth and distribution patterns in the barrel fields alone. To seek the transcriptomic drivers, we developed NuNeX, a method for isolating nuclei from fixed tissues, to explore sorted VChIs. This highlighted differentially expressed neuronal structural transcripts, altered exitatory innervation pathways and established Elmo1 as a key regulator of morphology following deprivation.

Keywords 3D; ChAT; deprivation; interneurons; reconstruction
Subject Category Neuroscience
DOI 10.15252/embj.2021110565 | Received 30 December 2021 | Revised 3 October 2022 | Accepted 17 October 2022 | Published online 15 November 2022
The EMBO Journal (2023) 42: e110565

Introduction

Neuronal morphology is defined by the distributions and composition of channels, synapses, dendritic and axonal processes, which determine the computational capabilities of specific neurons and their impact on neuronal circuits (Eyal *et al*, 2014; Markram *et al*, 2015; Beniaguev *et al*, 2021; Cuntz *et al*, 2021). Correspondingly, numerous studies have strived to achieve an accurate reconstruction of these neuro-morphological features (Peng *et al*, 2015), and immense efforts have been devoted to precisely define absolute values of the measured parameters (e.g., dendrite diameter and length, neurites per cell and axonal span; Kasthuri *et al*, 2015; Motta *et al*, 2019; Antonopoulos *et al*, 2021). These features are subject to dynamic changes, in response, for example, to stressful experiences (Maravall *et al*, 2004; Farrell *et al*, 2016), viral infection (Jurgens *et al*, 2012), or disease (Moolman *et al*, 2004). However, tools and statistical frameworks for studying populations of neurons and their alterations following biological and experimental perturbations remain limited. This is primarily due to the time-consuming manual/semi-manual nature of neuronal reconstructions, which are also prone to bias due to technical variability that comes from tissue or instrument variability and human tracing errors. Compared with other high-throughput techniques (e.g., Single-Cell/Nuclei RNA-Seq; Habib *et al*, 2017; Li *et al*, 2019), manual neuronal reconstructions offer limited statistical power and fail to detect fine cumulative differences in neuronal features across experimental conditions. Furthermore, limited numbers of reconstructions per mouse hamper the prospects of correcting for sample variability and batch effects in neuronal population studies.

Recent improvements in tissue clearing (Renier *et al*, 2014; Susaki *et al*, 2014; Tomer *et al*, 2014), light-sheet imaging

1 The Edmond and Lily Safra Center for Brain Sciences (ELSC), The Life Sciences Institute, The Hebrew University of Jerusalem, Jerusalem, Israel
2 The Department of Biological Chemistry, The Life Sciences Institute, The Hebrew University of Jerusalem, Jerusalem, Israel
3 The Department of Neurobiology, The Life Sciences Institute, The Hebrew University of Jerusalem, Jerusalem, Israel
4 Department of Biology, Stanford University, Stanford, CA, USA
5 Sorbonne Université, Paris Brain Institute - ICM, INSERM, CNRS, AP-HP, Hôpital de la Pitié Salpêtrière, Paris, France
6 Biochemistry and Organic Analytical Chemistry Unit, The Institute of Medical Research and Occupational Health, Zagreb, Croatia
*Corresponding author. Tel: +972 54 882 0629; E-mail: hermona.soreq@mail.huji.ac.il

RIGHTSLINK Copyright Clearance Center ...hed under the terms of the CC BY NC ND 4.0 license.

(Chakraborty *et al*, 2019), and image processing techniques (Cuntz *et al*, 2010; Quan *et al*, 2016; Renier *et al*, 2016; Murakami *et al*, 2018) now enable high-resolution imaging from entire neuronal populations in large brain regions.

The mammalian cortex receives cholinergic input from two major sources: deep nerve growth factor (NGF)-responding basal nuclei projection neurons (Satoh *et al*, 1983) and local cortical interneurons expressing vasoactive-intestinal polypeptide (VIP) and choline acetyltransferase (ChAT; von Engelhardt *et al*, 2007): the VIP/ChAT interneurons, or VChIs. Relatively little is known about VChIs molecularly, functionally, and morphometrically. In previous works, VChIs have been described as sparse, bipolar neurons, mostly distributed in cortical layers 2/3 (Saunders *et al*, 2015; Li *et al*, 2018; Dudai *et al*, 2020). Single neuron RNA-sequencing (RNA-seq) analyses have indicated VChI's reactiveness to immune-related neurokines (Lobentanzer *et al*, 2019; Granger *et al*, 2020). Notably, VChIs co-release GABA and acetylcholine (ACh), and possess diverse capacities to modulate the activity of neighboring neurons (Saunders *et al*, 2015; Obermayer *et al*, 2020). We have demonstrated VChI modulation of cortical somatosensory responses *in vivo* and showed that they receive direct input from nucleus basalis projection neurons (Dudai *et al*, 2020). However, the structural diversity of VChIs and its links to the long-term dendritic and transcriptomic plasticity of these neurons remained largely unknown and became the focus of our current research.

To assess the morphological complexity of VChI populations in naïve and experimentally manipulated mice, we established the Population Reconstruction Pipeline (PopRec), an analysis pipeline that enables unbiased quantifiable automatic reconstructions of neuronal populations. We focused on VChIs in the mouse barrel cortex, a well-defined anatomical region, which is one of the most central sensory systems in the mouse brain and serves as a model of morphological plasticity (Feldman & Brecht, 2005). The barrel cortex occupies a large fraction of the mouse sensory cortex, receiving inputs from individual whiskers in dense anatomical areas, called "barrel fields" (Lendvai *et al*, 2000; Petersen, 2007). To date, and as far as we are aware, no large-scale study has qualified morphological differences in interneuron populations in the barrel cortex. Hence, whether and how this class of neurons responds to sensory deprivation remained obscure.

As the barrel cortex functioning is directly modulated by cholinergic signaling (Eggermann *et al*, 2014; Lin *et al*, 2015) and whole-brain profiling demonstrated that VChIs are particularly enriched within the barrel cortex regions (Li *et al*, 2018), we sought to ask whether and how VChIs respond morphologically and transcriptionally to mild, unilateral whisker deprivation admitted at a young age.

Our working hypothesis predicted that exploring the relationship between the morphology and transcriptomic profile of a neuron population might reveal clues to how neurons grow, adapt, and function (de la Torre-Ubieta & Bonni, 2011; Gutierrez & Davies, 2011). However, since neurons are highly intertwined, postmitotic cells, they do not react well to the physical strains accompanying standard dissociation protocols (Altman *et al*, 2016). This limitation worsens as the brain matures and the properties of the extracellular matrix change, limiting most studies to the isolation of nuclei from the mature brain (Habib *et al*, 2016), which do not retain a fluorescent signal for FACS enrichment. In order to overcome this limitation and evaluate which transcriptomic alterations accompany the morphological changes in barrel cortex VChIs, we developed NuNeX; a robust, simple, and rapid method for Fluorescent Activated Cell Sorting-based (FACS) isolation of neurons expressing a fluorescent protein from the adult mouse brain.

Results

The PopRec pipeline

We describe a sequence of experimental and analysis steps enabling to reconstruct the somatic coordinates and the dendritic morphology of the VChIs population in the mouse barrel cortex (Fig 1).

To specifically label VChIs, we crossed C57Bl6 mice expressing Cre recombinase under the control of the endogenous choline acetyltransferase (ChAT) gene (ChAT-IRES-Cre) with an Ai14 reporter mouse (LoxP-Stop-LoxP-tdTomato), creating ChAT-CreXAi14 mice expressing a red fluorescent protein in all cholinergic neurons. We perfused mice from the same litter, isolated their cortices, processed them according to the iDISCO$^+$ protocol (Renier *et al*, 2014) for imaging with light-sheet microscopy and acquired both autofluorescence and fluorescence signals spanning the entire barrel cortex region (Fig 1A, Movie EV1).

Across-sample image normalization

Large-scale tissue clearing and imaging introduce technical signal variability both within and between biological samples. To compare variable dendritic signals of VChIs between cortical samples, we

Figure 1. Scheme of the PopRec analysis pipeline for generation and evaluations of automatic reconstructions.

A ChAT-CreXAi14 mice were sacrificed, perfused, and cortices were isolated and subjected to iDISCO$^+$ clearing and light-sheet imaging.

B PopRec pipeline preprocessing: Across-sample signal intensity correction with the intensify3D$^+$ App. Intensity gradient correction: Precorrection (red frame); post-correction (blue frame); Intensity profiles correspond to yellow horizontal lines. Across-sample intensity was corrected by mean pixel histogram equilibration.

C PopRec pipeline step 1: automatic soma detection and data augmentation into high-resolution mini-cubes around each cell together with neighboring cells and dendrites with the Soma-to-Cube App.

D PopRec pipeline step 2: feeding every mini-cube to a computer cluster node together with a combination of two reconstruction parameters (maximal point gap distance (MPD) and fluorescence threshold (Thr)) with the Neuron reconstruction App (Architecture based on Trees Toolbox competitive reconstruction) while accounting for close proximity somata.

E PopRec pipeline step 3: feature extraction (BlueBrain/NeuroM) and ranking of candidate reconstruction in a randomized manner with the Reconstruction validation App where the user decides if the current reconstruction displayed is accurate or not with full 3D visualization of original imaging.

F The output of the PopRec pipeline produces the reconstruction cubes, neuronal reconstructions, a list of features from the reconstructed neurons, and the predicted rank of each neuron in the training dataset. In this study, we used this subset rank to train a regression model (MATLAB) and filter out neurons that do not pass a certain quality threshold from downstream analysis.

Downloaded from https://www.embopress.org on December 26, 2023 from IP 132.64.53.73.

 © 2022 The Authors

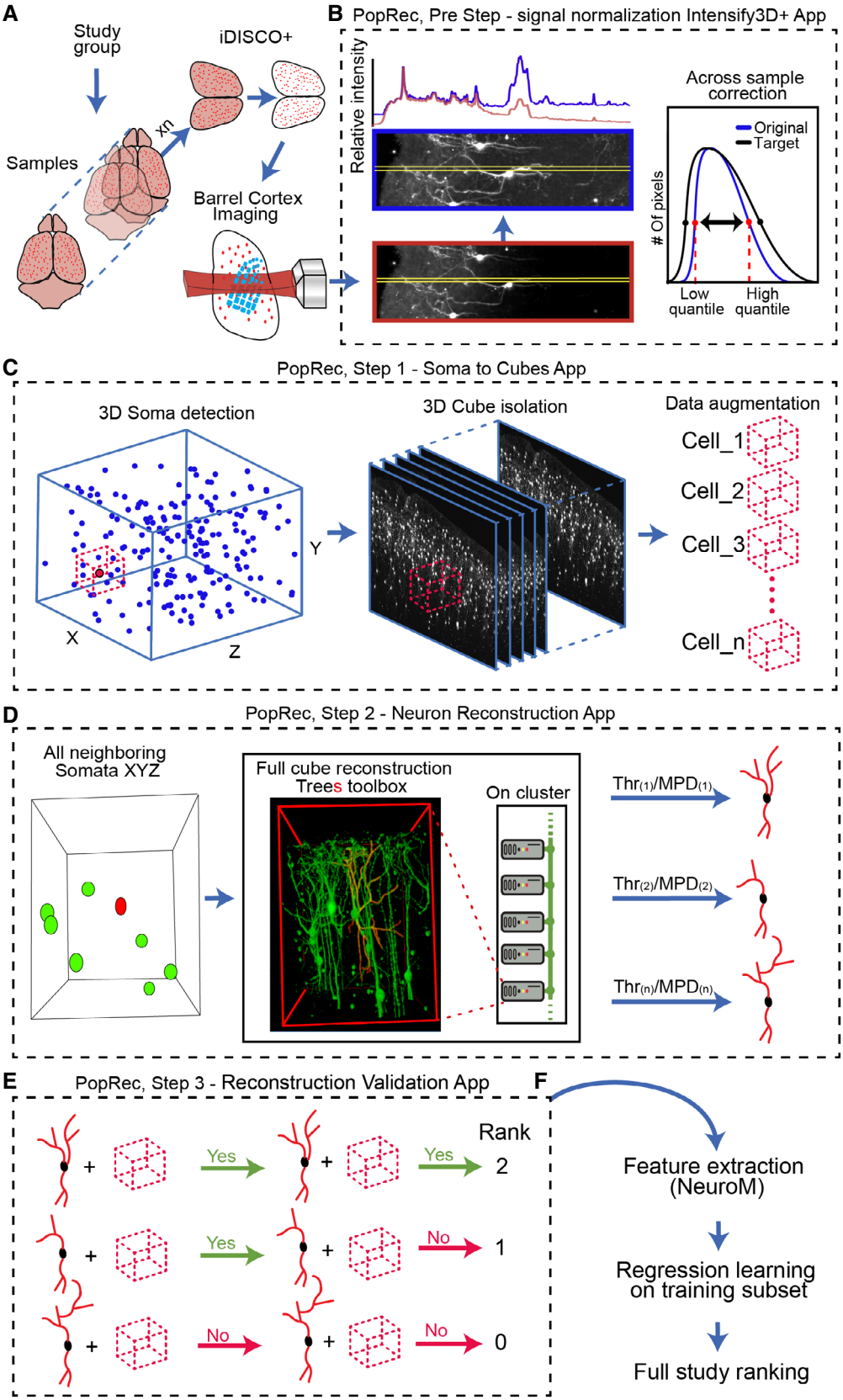

Figure 1.

Downloaded from https://www.embopress.org on December 26, 2023 from IP 132.64.53.73.

RIGHTSLINK

constructed an updated version of our in-house 3-dimensional normalization tool (Yayon *et al*, 2018; Intensify3D$^+$, (Appendix Fig S1), https://github.com/nadavyayon/Intensify3D) and corrected the observed signals within and between biological samples (Fig 1B).

Data augmentation to smaller 3D volumes

Postnormalization, we applied another application—Soma to Cubes. This Application first automatically detects the soma locations based on predefined parameters. Subjecting the imaged volumes to this Application enabled the automatic detection of VChI somata with an accuracy of 97.94 ± 0.012% determined by manual validation (14 cortical samples of naïve mice, Fig 1C, Dataset EV1, see Materials and Methods).

Current tracing and reconstruction tools are often limited by imaging size and have significant RAM limitations (BitPlane-IMARIS Filament Tracer, neuroGPS; Quan *et al*, 2016). To overcome this challenge, we developed a data augmentation approach by isolating "mini-cubes" that were ~ 350 × 550 × 350 pixels in size in this study (Materials and Methods) and are centered around each of the detected somata. The cube size was selected to be large enough to span major dendrites of the center neuron and a few surrounding neurons in one mini-cube (Fig 1C, Appendix Fig S2).

Single neuron automated reconstructions

After data augmentation to 3D cubes, the Neuron Reconstruction App uses each of these 3D images and the corresponding coordinates of all somata in the analyzed cube as its input. All neurons in the cube are simultaneously reconstructed to minimize large reconstruction errors, since the core reconstruction algorithm, which is based on the Trees Toolbox, takes surrounding neurons into account when traced in a competitive manner (Cuntz *et al*, 2010). PopRec also supports automatic reconstruction in a CPU cluster with a custom-built input–output interface (see codes). Thus, all neurons could be reconstructed in parallel (Fig 1D, Appendix Fig S3).

Mimicking the decision-making process of different human tracers and aiming to enhance the robustness of these reconstructions, the reconstruction App generates multiple versions of each neuron by a factor-combination of two basic reconstruction parameters: (i) The maximal distance between two points, and (ii) The fluorescence threshold in each version. In addition to reconstructions, this App also extracts multiple morphological features (NeuroM https://morphio.readthedocs.io/en/latest/specification.html, Dataset EV2) from each version of the center neuron.

Randomized reconstruction ranking

To quickly review and rank thousands of neuronal reconstructions by the experimenter in a double-blinded, randomized manner across all samples in an experimental dataset, we built the last App in the PopRec pipeline—Reconstruction Validation App. This tool presents the neuron reconstruction with the original image in a one-by-one manner, both in the interactive 3D format. This review process can be run multiple times on the same neurons and when completed, it ranks the accuracy of each reconstruction by the number of times that neuron was reviewed (Fig 1E, see Appendix Fig S4 for more information).

We used this ranking to train a MATLAB classifier based on the morphological features and ranks for all of the neuron reconstructions (including multiple versions of each neuron), which allowed to both "clean out" poorly reconstructed neurons and also select the best versions of high-accuracy reconstructions (Fig 1F).

To estimate reconstruction accuracy for the PopRec pipeline relative to the actual image in a manner detached from the analysis pipeline, and to evaluate a substantial fraction of the tested population, we manually examined ~ 300 out of ~2,400 neuron reconstructions from the seven naïve ChAT-CreXAi14 mice, overlaid the actual reconstruction with the original image and scored each reconstruction as follows: (i) "Full length," where the reconstruction accurately represented the major dendrites (proximal and distal arborizations), (ii) "basic structure"—where the major neurites were accurate, except for some tracing errors, which occurred in distal dendrites, assigning either too many or too few dendrites to the reconstructed neuron, and (iii) "significant errors"—where the neurons presented significantly missed tracing of major stem dendrites (SD). We found full-length accuracy in 71.7% (228/318), fine structure errors in 22.3% (71/318), and significant errors in 6% (19/318) of the analyzed cells.

We defined SD as the full dendritic trees that reside from the soma: a bipolar neuron would have two SD and multipolar more than two. Overall, the PopRec approach hence yielded 94% accuracy in terms of basic neuron morphology and 72% accuracy in terms of the fine dendritic details (Dataset EV3, Movie EV2).

Mapping cells to the barrel cortex region

Little is known about the morphology and distribution of specific VChI sub-populations. However, previous reports suggested the existence of two distinct morphological sub-populations: bipolar/bitufted and multipolar (Consonni *et al*, 2009; Li *et al*, 2018; Granger *et al*, 2020). Since VChIs are enriched in somatosensory cortical regions, we focused on characterizing the VChIs within the mouse barrel cortex. To identify the true location of the barrel field regions in 3D from each cortical region, we investigated the autofluorescence signal from iDISCO-cleared brains, which is especially indicative of tissue density and white matter composition. We normalized the autofluorescence signal (Fig 2A) with Intensify3D$^+$ and used these corrected images to: (i) 3D render and precisely measure the surface (top) and corpus callosum (bottom) boundaries of the barrel cortex region (Fig 2B), and (ii) 3D render and measure the region surrounding the barrel fields (Fig 2C). Overlaying the 3D ROI of the barrel fields with the locations of individual somata allowed us to define the location of each neuronal soma in respect to the barrel cortex (Fig 2D, Movie EV3) and to measure the exact somatic depth of these VChIs.

Morphological classification of barrel cortex VChIs

After having established the location of the barrel cortex and registration of VChIs within these regions, we next profiled the morpheome of VChIs within and between mice by employing the PopRec pipeline for n = 2,383 VChIs in 14 cortical hemispheres from seven mice (Fig 3A). Clustering of extracted morphological features (Materials and Methods) by t-distributed stochastic neighbor embedding (tSNE) revealed two distinct morphological clusters. Correspondingly, we identified these two primary clusters as dominated by (i) cells with two principal SD—bipolar VChIs (biVChI), and (ii)

Downloaded from https://www.embopress.org on December 26, 2023 from IP 132.64.53.73.

 © 2022 The Authors

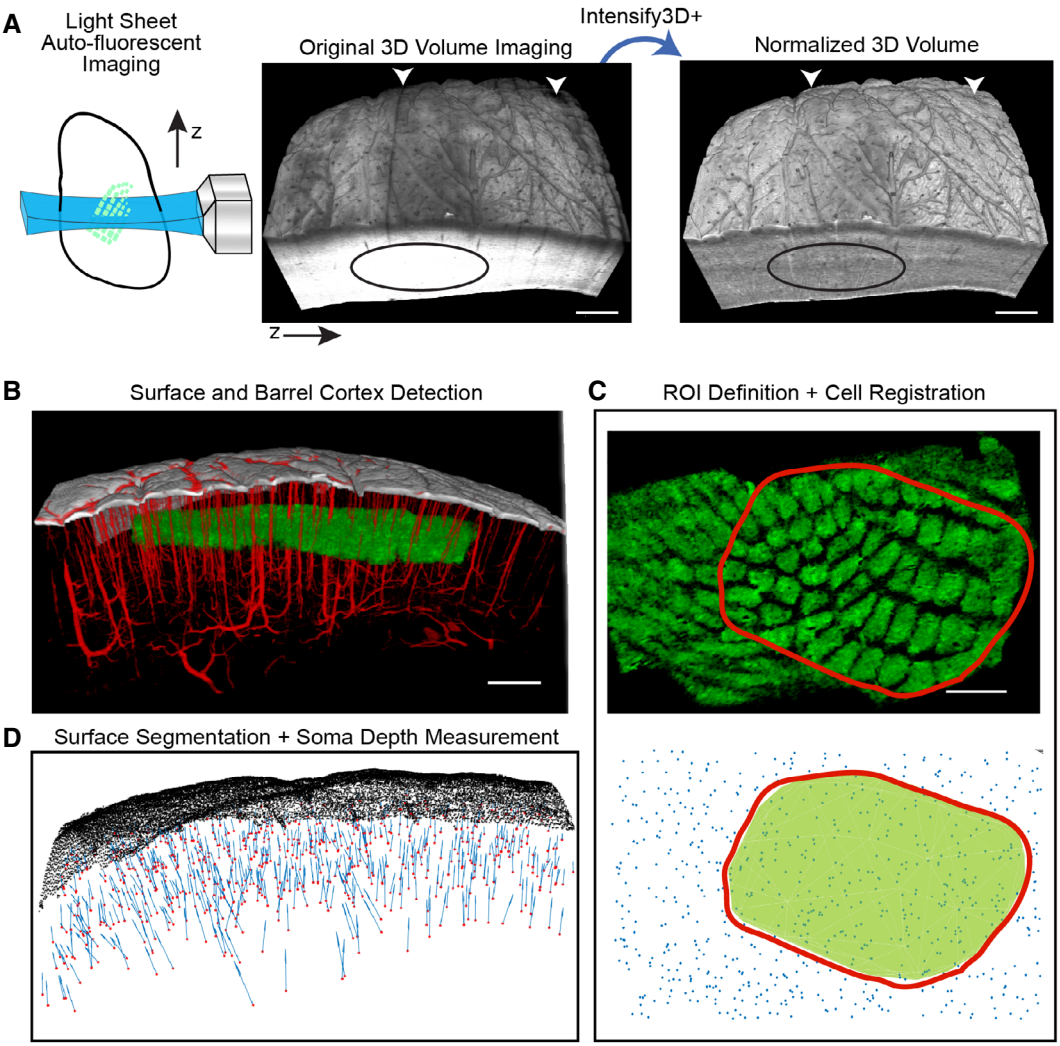

Figure 2. Definitions of the barrel cortex region and registration of VChI somata to volume.

A Scheme of light-sheet autofluorescence imaging of the barrel cortex region and Intensify3D^{+} normalization of autofluorescence pixel histograms, which corrects 3D light-sheet scanning artifacts (white arrows) and variable intensity (black ellipse) in a tissue volume. Scale bars: 0.5 mm.

B Volume rendering of images postnormalization used to isolate the cortical surface and estimate the boundaries of barrel regions (green) without any additional staining, large blood vessels are depicted in red. Scale bars: 0.5 mm.

C A 3D barrel cortex region of interest (ROI) area (top—red line) is manually measured and segmented (FIJI) to define an anatomically based ROI (bottom). This ROI is used to determine for all neuronal somata (blue dots) whether they are located within or outside of the barrel cortex. Scale bars: 0.5 mm.

D 3D registration and mesh segmentation of VChI somata to the cortical surface. The minimal Euclidean distance and direction (blue arrows) to the surface are calculated for each of the neuron somata (red dots).

cells with three or more principal SD termed multipolar VChIs (mVChI; Fig 3B and C). Importantly, we noted consistent segregation into two VChI sub-populations across individual mice, independent of sex and cortical side (Appendix Fig S5). Depth measurements (normalized depth between surface and white matter) mapped most VChIs in the predicted depth of cortical layer 2/3 and identified a second significant distribution of VChIs in layer 4. Furthermore, the two sub-populations were differentially distributed as a function of cortical depth: biVChIs were homogeneously and almost exclusively distributed in layer 2/3, whereas mVChIs were divided between layers 2/3 and 4. (Fig 3D). To further validate the dichotomy in VChI populations, we performed an independent 3D Sholl analysis (Sholl, 1953) of biVChIs and mVChIs. This measurement, which was not included as a feature for tSNE clustering, showed that biVChIs had less proximal and more distal branching, at least up to 240 μm from the cell soma. In comparison, mVChIs showed more proximal but less distal branching (Fig 3E), indicating that the total dendritic length of biVChIs and mVChIs might be subjected to a constraint that limits the maximum cumulative dendritic length of VChIs at large. Of note, these considerations are limited to the 3D extracted cube surrounding each neuron (~ 350 × 550 × 350 px^3, xy pixel size – 0.816 μm, z-step – 1 μm), and possible differences between these cell clusters could exist for dendrites extending beyond 240 microns from the soma.

Downloaded from https://www.embopress.org on December 26, 2023 from IP 132.64.53.73.

RIGHTSLINK

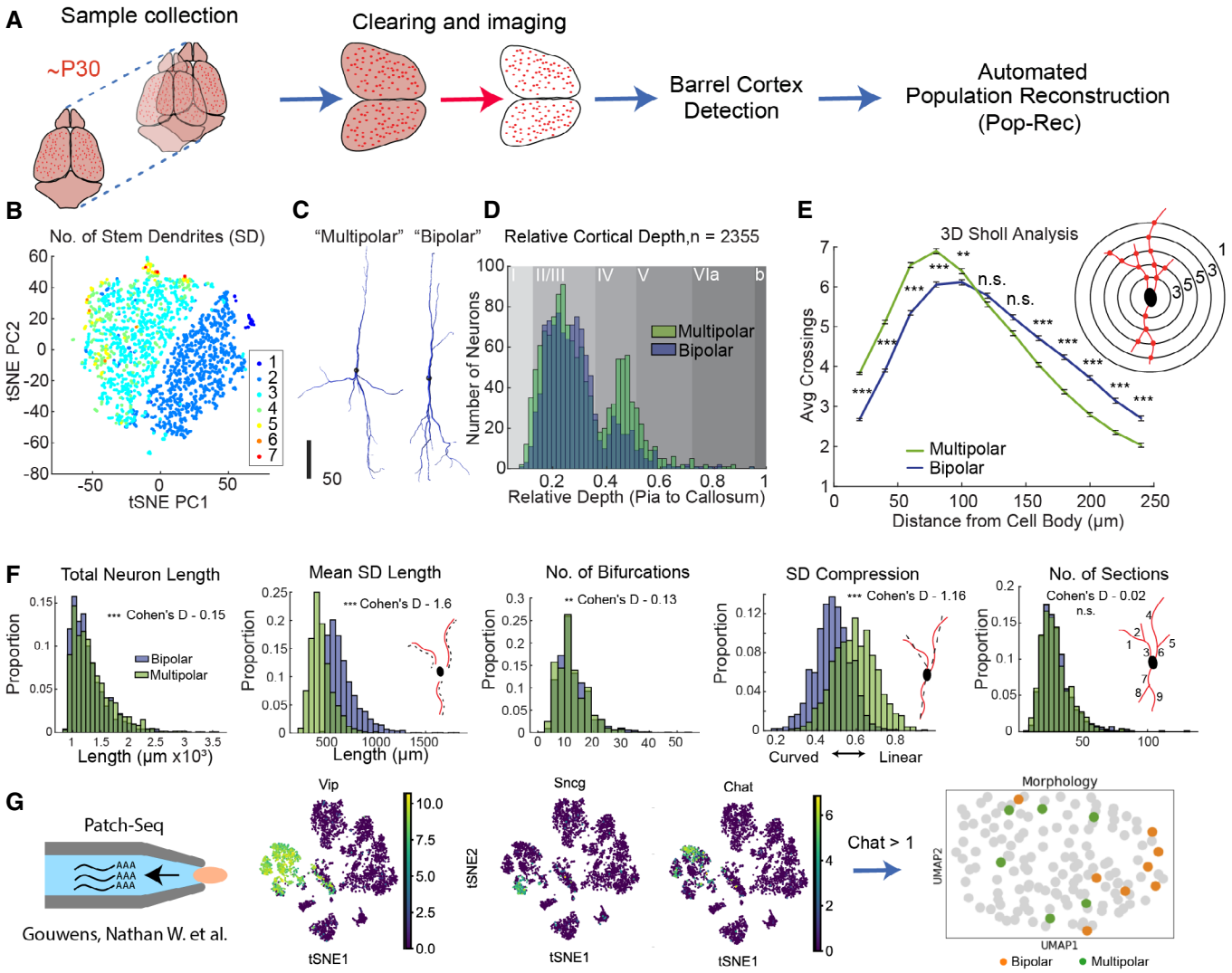

Figure 3. Segregating VChIs into bipolar (biVChI) and multipolar (mVChI) morphologies.

A Sample collection: naïve mouse cortices were processed, the barrel cortex area was defined, and VChIs were subjected to the PopRec pipeline.

B tSNE clustering by morphological features. Colors represent the number of stem dendrites or dendritic trees originating from the cell soma.

C Representative bipolar (left) and multipolar (right) VChIs of each group. Horizontal scale bar: 100 μm.

D Cortical depth distribution of biVChIs (blue) and mVChIs (green) measured automatically by soma detection.

E 3D Sholl analysis of biVChIs and mVChIs (Bonferroni corrected linear mixed effects, LME, error bars represent SEM+-). Example of Sholl analysis and number of intersections (right). Bars represent the standard error of the mean.

F Distribution of biVChIs vs mVChIs for total neuron length, mean stem dendrite length per neuron, mean number of bifurcations per neuron, stem dendrite (SD) compression as a measure of dendrite curvature, and the total number of sections per neuron. See Dataset EV4 for full statistical description.

G PatchSeq analysis of VChIs. UMAP embedding of expression profiles from the entire study highlighting marker genes for inhibitory interneurons. Bottom right—only ChAT-positive neurons out of which 14 VChIs from layer 2/3 ($n = 8$ bipolar and $n = 6$ multipolar) labeled as bipolar and multipolar.

Data information: In (D–F) linear mixed effects (LME) models were used in all panels unless stated otherwise. $n = 7$ mice in total with 14 cortical hemispheres. $n = 2{,}355$ total cells, n-bipolar = 1,016, n-multipolar = 1,339. ***$P < 0.001$, **$P < 0.01$, *$P < 0.05$. Cohen's $D < 0.2$ = small effect, $0.2 < D < 0.5$ = medium effect, $D > 0.8$ = large effect.

Specifically, biVChI and mVChI clusters presented fundamentally distinct morphological features. For example, the SD compression feature that provides a measure of SD linearity was larger in mVChIs (beta = 0.1 ± 0.0043) than that in biVChIs. In comparison, the SD were shorter in biVChIs (beta = −235.44 ± 7.13 μm), such that the cumulative length of all SD in mVChI and biVChI was similar (Fig 3F).

Next, we explored online PatchSeq datasets that included all major inhibitory cortical interneurons in the visual cortex (Gouwens *et al*, 2020). Out of 141 ChAT-positive layer 2/3 cells (> 1 read), 14 had reconstruction data. Interestingly, in the dimensionality-reduced UMAP space, single bipolar and multipolar cells were separated according to their transcriptomic profiles alone, indicating a divergence in gene expression between these cell types (Fig 3G).

Downloaded from https://www.embopress.org on December 26, 2023 from IP 132.64.53.73.

© 2022 The Authors

However, the low number and experimental constraints did not allow us to assess specific genes or pathways as particular to these cell type sub-populations. We conclude that the barrel cortex biVChIs and mVChIs differ in their cortical distribution, in their proximal and distal dendritic branching patterns, and in their transcriptomic profiles, compatible with distinct innervation features and potentially unique functions of these two VChI types in the cortical microcircuits (See Dataset EV4 for full feature statistics).

Whisker deprivation induces long-lasting morphological alterations of VChIs in both contra- and ipsilateral cortices

During a critical period in early mouse development, individual neuronal types in the mouse barrel cortex have been reported to respond to the deprivation of sensory inputs to the barrel cortex by distinct morphological changes (Maravall *et al*, 2004; Chen *et al*, 2012). However, although this form of dendritic plasticity has been extensively studied, specific morphological changes in non-pyramidal neurons and inhibitory neurons were not systematically quantified nor studied in detail for any neuron type at the population level. To fully characterize the structural response of VChIs to mild sensory deprivation, we exposed young ChAT-CreXAi14 pups (p7) to a single event of light anesthesia with or without unilateral plucking of their full whisker pads. After 21 days we executed the complete imaging and PopRec pipeline (Fig 4A) to characterize those barrel cortex VChIs that were derived from sensory-deprived animals. We defined three experimental tissue backgrounds: (i) The barrel fields from the contralateral hemisphere to the deprivation side, where we expected to see the most significant influence of deprivation, could be right or left (See Fig 4A for circuit diagram), (ii) The barrel fields in the ipsilateral hemisphere to the deprivation side, and (iii) The barrel fields from un-deprived mice from either hemisphere. tSNE analysis of VChI morphology features re-captured the distinction between bipolar and multipolar VChIs (Fig 4B). However, following whisker deprivation, we observed a shift in the proportion from biVChIs to mVChIs, in contralateral cortices but strikingly, also in ipsilateral cortices from whisker-deprived compared with control mice. Further, we observed a similar shift in the cortical depth distributions of VChIs, with a higher proportion of deep VChIs (Fig 4C and D). Both biVChIs and mVChIs from whisker-deprived mice showed more elaborate branching and extended dendrite sections, and less curved dendrites compared with control mice; however, mVChIs showed more prominent dendritic differences (Fig 4E, Dataset EV5).

To estimate differences between experimental conditions at the level of the single cells, we trained a Gaussian regression model (MATLAB) with 20-fold cross-validation to separate cells according to their condition. Similar to individual feature differences, these characteristics were evident in both the ipsi- and contralateral hemispheres while showing a stronger divergence in the contralateral side (Fig 4F). To probe if the spatial order and scattering pattern of VChIs was affected by deprivation, we measured the expected distribution of cell somata in the 3D space and found that in both ipsi- and contralateral hemispheres, VChIs in deprived mice showed a more clustered, less random distribution compared with control mice (Fig 4G). Finally, to ask whether the observed effects were specific to the barrel regions, we estimated morphological differences in peripheral VChIs of the barrels by only including cells that are in the 20% periphery of the barrel fields. We found no difference between bipolar to multipolar proportion, contrary to what we observed inside the barrel regions, and as a whole, all changes were only observed between the control and deprived mouse and not within the deprived mouse itself (Fig 4H, Dataset EV10). This points again to localized, barrel-specific alterations in cell morphology in addition to global, mouse-level alterations following deprivation.

In summary, our findings show that unilateral deprivation affects VChIs in both hemispheres, causing a shift between VChI subpopulation types and altering their dendritic features. Interestingly, VChIs in cortices of whisker-deprived versus nondeprived mice differ more than those in the ipsi- and contralateral hemispheres of whisker-deprived mice. Considering that the two cortical hemispheres are heavily connected by excitatory afferents (Oh *et al*, 2014), this might reflect a situation in which sensory deprivation of one hemisphere partially deprives the other. This shift in soma depth distribution and general cell scattering, to the best of our knowledge, is the first example of such an effect, following a single event of mild whisker deprivation; and it might further indicate altered VChIs differentiation under reduced general input to layer 4.

Novel neuronal isolation method followed by RNA-sequencing reveals modified dendrite structure-related transcripts following whisker deprivation

Our current understanding of the relationship between neuronal morphological features, transcriptomic profiles, and developmental stressors is limited. Several genes, including neurotrophic factors (Horch *et al*, 1999) and transcription factors during development

Figure 4. Bi-hemispheric effects of mild whisker deprivation on barrel cortex VChI morphology.

A Experimental scheme: mice were subjected to a single event of anesthesia with or without unilateral whisker plucking at p7. Mouse brains were collected at p30 and subjected to the PopRec pipeline.
B tSNE clustering of whisker-deprived mice and controls.
C Observed shift in cell type proportion and depth distribution in both ipsi- and contralateral hemispheres (cross tab test with *post hoc*).
D Cell depth distributions from all three experimental conditions; notice the increased proportion of deep VChIs in whisker-deprived mice. Dashed line marks 0.38 relative depth (surface to callosum).
E Specific features of mVChIs and biVChIs to whisker deprivation (Linear mixed effects, error bars represent SEM+-).
F Regression model for predicting cortical condition at the single-cell level. Left—prediction value for each cell. Top right—confusion matrix for classification of neurons to condition chance level is 33%. Bottom right—prediction summary histogram.
G Ripley's L statistics for spatial distribution in 3D as a function of relative distance.
H Peripheral barrel selection and proportion of bipolar and multipolar VChIs as well as depth distribution of peripheral VChIs (Dataset EV10, Cross tab test with *post hoc*).

Data information: $n = 12$ mice in total with 24 cortical hemispheres as depicted in (A). ***$P < 0.001$, **$P < 0.01$, *$P < 0.05$. (A–F) n-bipolar = 1,167, n-multipolar = 1,561 neurons inside the barrel region (Dataset EV5). (G and H) n-bipolar = 426, n-multipolar = 517 neurons in the barrel periphery region (Dataset EV10).

Downloaded from https://www.embopress.org on December 26, 2023 from IP 132.64.53.73.

RIGHTSLINK

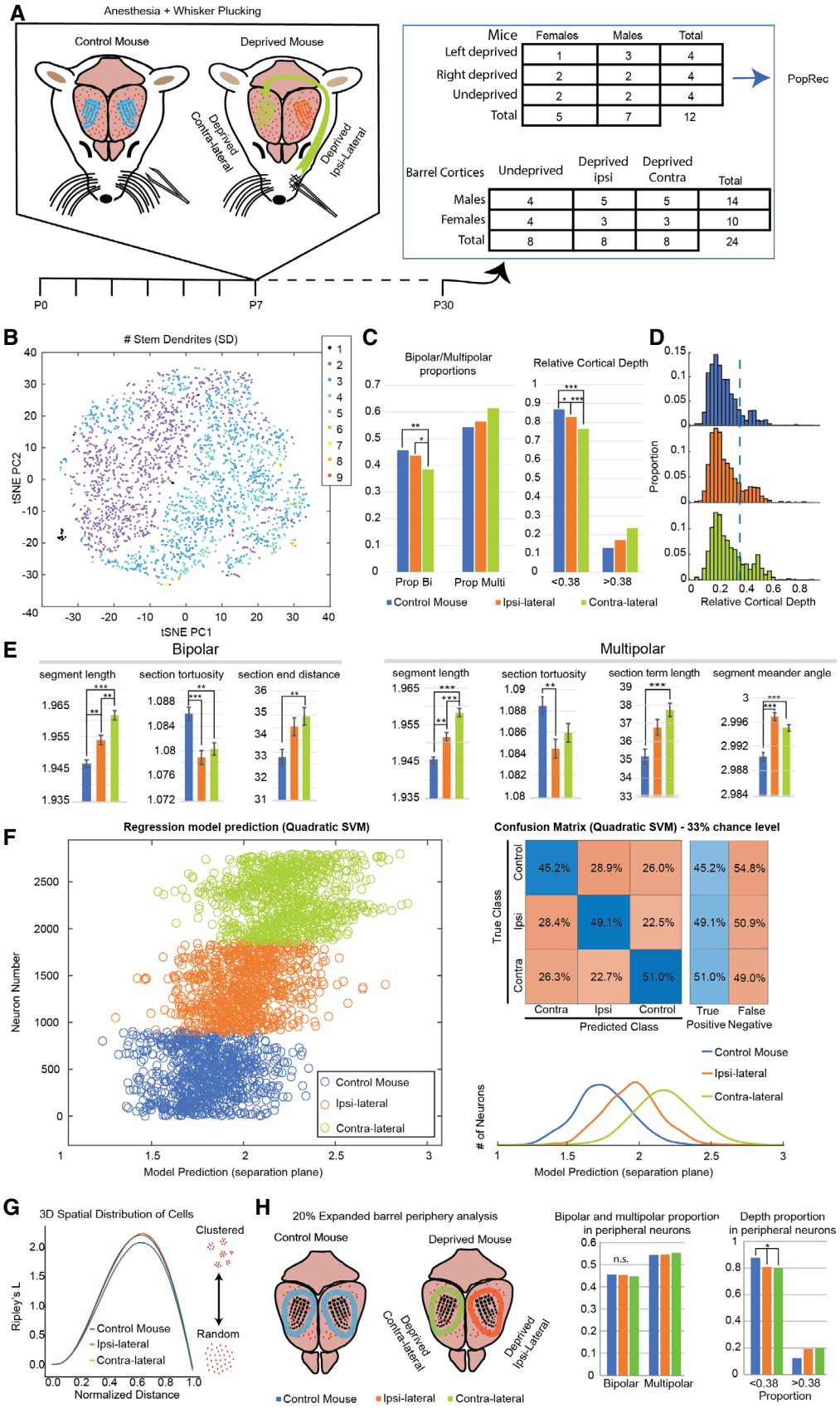

Figure 4.

Downloaded from https://www.embopress.org on December 26, 2023 from IP 132.64.53.73.

© 2022 The Authors

(Liu *et al*, 2013) are known to affect specific morphological features of axons, dendrites, and dendritic spines in particular subpopulations of cortical neurons. However, the general links between neuronal structures, the corresponding transcriptomic profiles, and the transcriptomic response to whisker deprivation remain largely unknown. Having observed consistent morphological alterations in dendritic structures in a mouse- and cortex-specific manner, we set out to determine whether those differences reflected modified transcriptomic profiles.

Focusing on VChIs provides a unique opportunity to track both morphological and transcriptomic profile shifts of a highly specialized neuronal population within a specific brain region. Given the sparsity of VChIs (which only constitute 0.5% of neurons in the barrel cortex; Dudai *et al*, 2020), low survival rates following isolation using standard enzymatic protocols, and the fact that standard nuclei extraction procedures (Habib *et al*, 2017) are robust, but incompatible with fluorescence-based detection of cytoplasmic proteins, we developed the NuNex method. This protocol is based on standard nuclear extraction but introduces a light fixation step prior to Dounce homogenization. We have found that this enables the preservation of fluorescently-tagged cytoplasmic proteins (Movie EV4) and cytoplasmic organelles while sustaining a high yield and quality of RNA from the preserved neurons (Appendix Fig S6). Performing this fixation step approximately 2 min postdecapitation limits secondary transcriptomic responses (e.g., apoptosis and expression of immediate early genes) during homogenization and isolation. We validated this method by FACS isolation of NeuN-positive and -negative cells and showed that the RNA quality and quantity were significantly higher compared with standard fresh nuclear isolation, particularly in NeuN-positive cells (Appendix Fig S6) via extraction with a dedicated kit (Materials and Methods). Furthermore, using NuNeX we were able to show high specificity of selected neuronal or glia marker genes by RT–qPCR (Appendix Fig S6).

To validate the applicability of the NuNeX protocol for isolating the ultra-sparse VChIs, we dissected cortical and striatal regions from naïve ChAT-CreXAi14 mice, applied the NuNeX procedure and performed FACS sorting of both tdTomato-positive and -negative cells (only DAPI-positive) from both regions (Appendix Fig S7). We tested the expression of key cholinergic components (the choline acetyltransferase ChAT gene and the vesicular acetylcholine transporter VAChT embedded within this gene) and tdTomato levels in FACS-sorted nuclear particles and found that within our preparations, both were exclusively expressed in the striatal and cholinergic interneurons. Furthermore, we validated our findings by matching the relative expression of ChAT and tdTomato based on immunolabeling and endogenous fluorescent quantification by confocal microscopy. Strikingly, we observed an almost 1:1 ratio between the levels of these proteins and their encoding RNAs (Appendix Fig S7).

Based on the concept that morphologically distinct neurons present transcriptionally distinct expression patterns, we predicted that RNA-seq profiles of specific neuronal populations, such as VChIs in mice subjected to whisker deprivation might disclose transcripts whose altered expression is reflected in the modified structure of those neurons. We hence sought transcripts and pathways whose expression is altered 3 weeks postdeprivation; the time point at which we assessed the morphological changes using PopRec (Fig 4). To study the transcriptomic response of VChIs to whisker deprivation, we performed the same unilateral whisker plucking procedure presented above, sacrificed the mice at p28 and immediately dissected cortical regions around the barrel cortex. Cortical tissues were subjected to the NuNeX protocol for isolating barrel cortex VChIs from both cortical hemispheres of mice that underwent unilateral whisker deprivation and controls (Materials and Methods). Samples were sorted by FACS based on DAPI and tdTomato signals. Due to the sparsity of VChIs, we pooled 1–4 cortices per sample to extract RNA and performed low input RNA library preparation and long RNA-sequencing (Fig 5A; Dataset EV6, and Materials and Methods). RNA-sequencing from VChIs isolated using our NuNeX procedure resulted in an average of 4.04e7 reads per sample (min = 2.49e7, max = 5.05e7 reads) and mean 62.2% mapping coverage (corresponding to an average of 2.51e7 mapped reads; min = 6.27e6 and max = 3.51e7 reads per sample, Fig 5D, Dataset EV6). Notably, the mean RIN was 7.2, reflecting good-quality RNA despite the relatively long isolation procedure (Fig 5B). Further, our extraction procedure enabled the detection of numerous cholinergic mRNA transcripts per sample, including transcripts of relatively low levels (e.g., ChAT and VAChT) and VIP-related transcripts, supporting the neuronal source of this dataset. Further, we compared the expression of preparations from control mice to known datasets and cortical cell type profiles (Dataset EV6) and found that NuNeX-isolated neurons from control mice were more

Figure 5. Transcript differences in enriched VChI populations following whisker deprivation.

A Experimental design and NuNeX RNA isolation strategy. Mice underwent unilateral whisker deprivation on day p7, were sacrificed on day 30 and their barrel cortices were isolated, lightly fixed, homogenized, and subjected to fluorescence-activated cell sorting (FACS). RNA was extracted from pool-sorted tdTomato and DAPI-positive neurons from left and right cortices of different mice, subjected to RNA-seq and downstream analysis.

B RNA-sequencing and mapping statistics.

C Correlation analysis of Cholinergic and VIP-related transcript profiles from control mice to a web-available dataset (Allen Institute) of 246 neuron types. ChAT/VIP neurons are most tightly correlated with bulk RNA profiles from control mice.

D Volcano plot depicting 110 DE transcripts between un-deprived (n = 4 pools of 1–3 mice, 8 samples – 4L, 4R) and deprived mice (n = 6 pools of 1–3 mice, 12 samples – 6L, 6R, DeSeq2 differential expression model).

E Pathway enrichment analysis of cellular compartments altered between control and deprived mice.

F siPools KD of Arpp21, Sam5b and Elmo1 transcripts in cultured primary neurons.

G Example images of Tuj1 labeled primary neurons under various KD conditions.

H Bar plots represent the expression of Elmo1 and Sema5b transcripts following KD of either transcript.

I Sholl analysis of primary neurons at 20–80 micron radius from soma center (ANOVA 1 with Tukey *post hoc* error bars represent SEM).

Data information: (A, B, D, E) n = 38 cortices from 18 mice in pools of 1–3, separated into 20 samples. (F–I) n is 33, 34, and 37 primary neurons for negative control (NC), Sema5b KD and Elmo1 KD, respectively. *$P < 0.05$, **$P < 0.001$, ***$P < 0.0001$.

Downloaded from https://www.embopress.org on December 26, 2023 from IP 132.64.53.73.

RIGHTSLINK

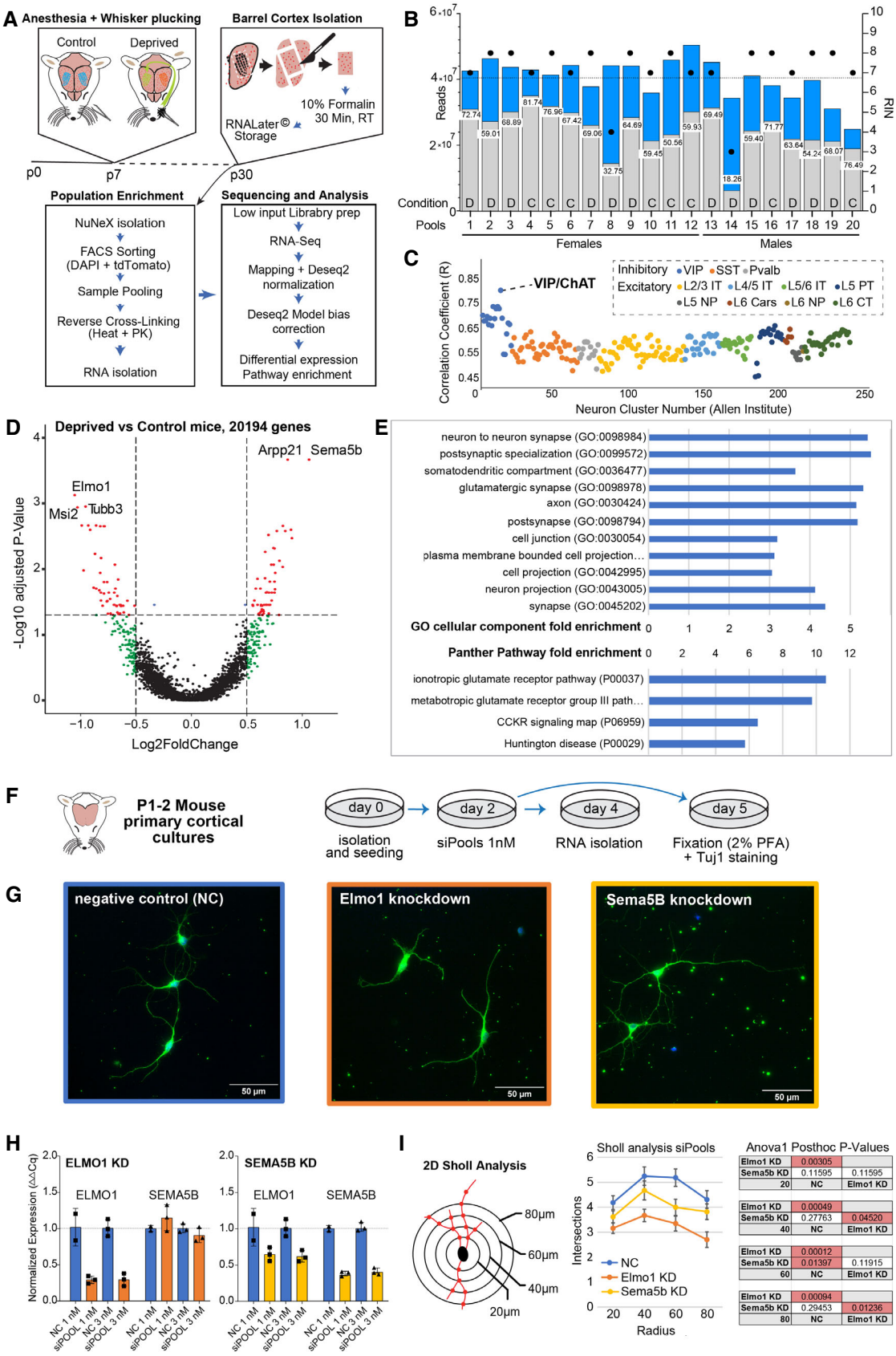

Figure 5.

Downloaded from https://www.embopress.org on December 26, 2023 from IP 132.64.53.73.

© 2022 The Authors

similar to the previously defined VIP/ChAT cluster (Allen institute) than to all other neuron clusters (Grubb test, $P < 0.01$; Fig 5C, Dataset EV7). By carefully controlling for the variability between transcriptomic profiles from the different tested pools and their distinct cortical sides (based on the Deseq2 batch correction model), we further identified bilateral differences comprising over 100 differentially expressed (DE) transcripts between deprived and undeprived mice, which were reproducibly detected as discriminating between these conditions. The top 5 DE transcripts were: Sema5b (log2 fold change [logFC] = 1.06, Benjamini–Hochberg–adjusted *P*-value, P_{adj} = 2.16e-4), Arpp21 (logFC = 0.87, P_{adj} = 2.16e-4), Elmo1 (logFC = −1.05, P_{adj} = 7.48e-4), Tubb3 (logFC = −0.96, P_{adj} = 1.11e-3), and Msi2 (logFC = −1.03, P_{adj} = 1.15e-3; Fig 5D, Dataset EV8). Of note, gene pathway analysis focused on coding genes (PANTHER; Mi *et al*, 2021) pinpointed the glutamatergic signaling pathway as significantly modified by past whisker deprivation, indicating sustained stress-induced alteration of glutamatergic input to cholinergic cortical neurons. A wider gene ontology analysis validated that the major cellular components that were affected were synapse and neuron projections (Dataset EV9). These indicate an altered genetic program in whisker-deprived mice, specifically in transcripts related to synaptic functions (Fig 5E). Intriguingly, the top two overexpressed genes, Arpp21 and Sema5b, and the top downregulated gene, Elmo1, were very recently found to play substantial roles in the branching of dendrites and axons, as well as in synapse stability and microtubule organization (Blazejczyk *et al*, 2017; Rehfeld *et al*, 2018; Jung *et al*, 2019; Table 1). Altogether, this analysis showed that a single mild whisker deprivation event during brain development causes a long-lasting shift in the transcriptional state of VChIs, which might contribute to modifying their morphology in a long-lasting manner dependent both on the initial insult and the affected hemisphere.

Finally, to test the global effect of altered Elmo1, Sema5b, and Arpp21 levels on neuronal branching, we performed a knockdown experiment targeting these transcripts in mouse cortical primary neurons (Fig 5F and G). Applying low levels of multiple target-specific antisense agents for Elmo1, Sema5b and Arpp21 (pools of siRNAs, siPools) resulted in suppression of Elmo1 and Sema5b transcripts by 71 and 64%, respectively. Implementing the siPools strategy, however, failed to downregulate Arpp21 (Appendix Fig S8). In addition, in cells with Sema5b knockdown, we observed a secondary decline of Elmo1 transcript levels (36% reduction; Fig 5H), which cannot be explained by sequence similarity. Elmo1 suppression further dramatically reduced the number of branching points throughout the dendritic Sholl analysis within 20–80 microns from the center of the soma (Fig 5I). Taken together, these findings establish a possible role for Elmo1 as a regulator of dendritic arborization and provide specific insights regarding the long-term effect of mild whisker deprivation on the input to VChIs.

Table 1. Known roles for differentialy expressed transcripts following whisker deprivation.

Gene name	Base mean	log2 Fold change	P_{adj}	Overexpression / depletion effect
Arpp21	4080.69	0.87	2.16E-04	Rehfeld *et al* (2018) ↑ Arpp21 ↑ Proximal branching ↓ Arpp21 ↓ Proximal branching
Sema5b	722.64	1.06	2.16E-04	Jung *et al* (2019) ~~Sema5b~~ ↓ Branch length ↑ Branching ↑ Sema5b ↓ Terminal branching ↑ Branch length
Elmo1	974.96	−1.05	7.48E-04	Blazejczyk *et al* (2017) ↑ Elmo1 ↑ Axon and filapodia length ↓ Spine numbers

Discussion

By constructing the structural "morpheme" of VChIs from control and whisker-deprived mice and seeking the corresponding RNA-seq differences, we found new links between the structural-transcriptomics features of VChIs while accounting for the corresponding experimental variability in multiple mice and extracting hundreds of spatially preserved cell structures per mouse. To challenge the validity of these VChI differences, we mined web-available single-cell transcriptomic datasets and performed experimental validation tests in cultured human-derived neuroblastoma cells (Appendix Fig S8), as well as murine primary neuronal cultures. Our approach enabled the exploration of the links between morphology, spatial distribution, and cellular transcriptomic differences at a single neuron resolution level, adding a new possibility of high-throughput neuronal morphology analysis and in-depth transcriptomic profiling.

Unbiased population reconstruction

Following the principles of large number statistics, our structural analysis approach is based on the concept that unbiased, multiple reconstructions from a neuronal population would converge to yield a true reflection of the transcriptomic-structural links in that population. In fact, the accuracy of single neuron structures can be compromised to an extent, if sufficiently large cell numbers are available for comparative analysis. As this assumption only holds true if the applied analysis is unbiased between all samples in the studied experimental group, we developed a computational correction approach for sample imaging bias (Intensify3D^{+}) within and between biological samples. Next, we developed a tool for fast 3D detection of neuron somata. We defined the entire barrel cortex of each hemisphere as our anatomically based region of interest (ROI) and subjected it to three-dimensional absolute measurements of neuronal cortical depths and structures. To enable the rapid automated reconstruction of thousands of neurons with multiple structural parameters, and to handle huge imaging datasets, we "broke down" the data into small "cube" pieces that could be analyzed as CPU clusters. As our approach keeps the original cortical coordinates of each neuron, it further enables regional analysis of neurons such as those residing in specific cortical columns. Our strategy is amenable to use with many other automated reconstruction tools for single neurons. Furthermore, transforming large image datasets to mini-cubes can assist in benchmarking the performance of machine learning reconstruction tools in a well-controlled manner. Notably, the size of these 3D cubes is critical for the type of questions explored. For example, if the cells are very sparse, e.g., from

Downloaded from https://www.embopress.org on December 26, 2023 from IP 132.64.53.73.

RIGHTSLINK

in-utero electroporation, then the cubes could potentially be very large. In a dense population, the number of possible errors from proximal neurons will increase, which therefore requires focusing on more proximal regions of the neuron.

The VChI morpheme in naïve mice

Previous studies have suggested the existence of two morphologically distinct VChI populations, proposed to reflect functionally different neuron subtypes (von Engelhardt *et al*, 2007), and noted higher numbers of multipolar VChIs in deep layers (Li *et al*, 2018). Indicating differential roles of those VChI sub-populations, we identified different dendritic branching patterns and cortical distribution of bipolar (biVChIs) and multipolar (mVChIs) neuron subtypes. By contrast, we found no difference between the total cumulative dendritic length of biVChIs and mVChIs, which might indicate that for a given metabolic state (RNA, protein, and lipid compositions), a neuron subtype could "decide" how to distribute its resources, but will always be limited in the maximum size and length of its total extremities. Importantly, such alternating economy might lead to distinct functional processing of the cortical microcircuit. To objectively pursue such a distinction while avoiding bias due to other objective measures (e.g., molecular, electrophysiological), one would have to sample and cluster many representatives of the studied population and then prove by independent techniques that it indeed differs from others. We hope that our current morphometric VChIs atlas will serve as a baseline for such future analyses while establishing the terminal resources of neuronal extremities as a global neuronal feature.

Morphological response to whisker deprivation

To detect changes in population morphologies, we must resolve sufficiently large numbers while maintaining high reconstruction accuracy. We challenged this possibility and studied VChIs following a mild, single event of whisker plucking (on p7), which is within the range of physiological manipulations that do not alter the barrel fields themselves (Erzurumlu & Gaspar, 2012; Li *et al*, 2018), and is also sometimes performed by mice as a social dominance signal (Sarna *et al*, 2000). We compared between VChIs of distinct barrel cortices residing from un-deprived littermates, ipsilateral to deprivation hemisphere, and the hemisphere contralateral to the deprivation hemisphere. We observed a shift in the ratio of biVChIs to mVChIs, as well as in the layering and distribution of VChIs. Specifically, both biVChIs and mVChIs from deprived animals showed more extensive branching, with longitudinally extended but less curved dendrite sections; but multipolar VChIs from such animals showed yet more prominent dendritic differences, especially more linear and extended dendrites as reported for other neurons (Maravall *et al*, 2004). This outcome might account for the relatively larger thickness and/or possibly accelerated experience-induced differentiation of cholinergic interneurons in layer 2/3. Interestingly, while the most prominent effects were in the expected, contralateral barrel field (which receives most of its innervation from the plucked whiskers), we saw quite a strong alteration in morphology in the ipsilateral barrel field as well. This observation was further affirmed when we measured VChIs outside the barrel fields, where we saw no significant morphological difference between the ipsi- and contralateral sides and only the alteration on the level of both sides remained. Future studies will be needed to find out if this outcome is due to deficient input during the critical developmental period and interaction between the hemispheres or is it a more global-related state (e.g., stress response). Also, future deprivation studies would possibly need to consider these global changes and not only treat the ipsilateral side as a pure control.

VChI transcriptomic response to whisker deprivation

We established a protocol for robust enrichment of the sparse VChI populations from deprived and un-deprived mice by light fixation (NuNeX). Followed by FACS sorting, this procedure enabled transcriptomic analysis, highlighting over 100 differentially expressed genes and correspondingly altered pathways in postdeprivation VChIs, which might reflect their altered morphological states. Of these, the top modified Arpp21, Sema5b, and Elmo1 transcripts have recently been shown to alter neuronal morphological features (Rehfeld *et al*, 2018; Jung *et al*, 2019). Also, entorhinal cortical thinning in Alzheimer's disease patients has recently been attributed to a single nucleotide polymorphism (SNP rs11129640) residing in close proximity upstream to the ARPP21 gene (Furney *et al*, 2011). Pathway enrichment analysis further highlighted the glutamatergic signaling pathway as the predominant one affected by deprivation and altering structural neuron and synapse pathways. Investigating the direct effect of the above transcripts on cell morphology, we found that in both human neuroblastoma and mouse primary neuron cultures, Elmo1 KD had altered cell shape and neuronal branching patterns; pointing to the centrality of this transcript in controlling cell morphology. While further investigation is needed to better link between the observed transcriptomic and morphological changes and disclose their cortical function, our current findings shed new light on the link between neuronal transcription and morphology and how they relate to each other.

Cholinergic implications for age and disease states

Cholinergic networks are notably subject to differences between sexes and changes in mental disease states (Lobentanzer *et al*, 2019), but the corresponding structure–function relationships are still unknown. Furthermore, large-scale studies demonstrate the elevated risk of dementia under prolonged exposure of aged individuals to anticholinergic medications (Coupland *et al*, 2019), and the cortical cholinergic innervation is severely impaired during the course of Alzheimer's disease (Geula & Mesulam, 1989). However, the corresponding changes in either the morphology or the transcriptomic profiles of cortical cholinergic interneurons remain unknown. Combined multi-omic approaches such as those developed in our current study may shed light on these observations and enable to link specific neuronal subtypes and genes to elements of human health and wellbeing.

Conclusions and future implications

We developed a multi-leveled strategy for studying the baseline atlas of defined VChI populations (PopRec), revealed their insult-induced plasticity in dendrite morphology, and disclosed their

Downloaded from https://www.embopress.org on December 26, 2023 from IP 132.64.53.73.

 © 2022 The Authors

morphological and transcriptomic resources via a novel method for neuronal single-cell isolation from fixed tissues (NuNeX). Recent advancements in the field of whole-brain clearing and light-sheet imaging on one hand, as well as spatial transcriptomics and single-cell RNA-seq from fixed tissues (e.g., from 10X Genomics or Parse Biosciences) on the other, offer exciting possibilities for using this approach with higher resolution and other neuronal populations. We hope that our work can serve as a basis for discussing the analysis and statistical approaches to morphological profiling of reconstructed neuronal populations, complementing other high-throughput single-cell resolution methods.

Materials and Methods

Mice

ChAT-CreXAi14 mice being C57Bl6 progeny mice derived from a cross of a loxP-Stop-loxP-tdTomato (Ai14 - Stock No. 007914, Jackson Laboratories) with ChAT-IRES-Cre mice (Stock No. 018957, Jackson Laboratories) were employed in this study.

Ethics statement

All experimental protocols were approved by the Ethics Committee for Maintenance and Experimentation on Laboratory Animals of The Hebrew University of Jerusalem (Ethics approval - NS-18-15456-3), Jerusalem, Israel, which follows the National Research Council (US) Guide for Care and Use of Laboratory Animals.

Whisker deprivation

For whisker deprivation experiments, ChAT-CreXAi14 p7 pups were lightly anesthetized with isoflurane (1–2% by volume in O_2, LEI Medical) for 1 min, then quickly removed from the anesthesia chamber and the entire whisker pad plucked individually with tweezers, or slightly pinched without plucking in control mice. After several minutes, once recuperated, treated pups were returned to the home cage and monitored until carried back to the parent cage. For labeling, on day p14 mice were ear-punched on the deprived side.

Perfusion and brain dissection for iDISCO clearing and immunostaining

At p30, ChAT-CreXAi14 mice, both control and whisker-deprived, were anesthetized with isoflurane as described above and administered an intraperitoneal injection of 200 mg/kg sodium pentobarbital until nonreactive. Following trans-cardiac perfusion with 1xPBS (5 ml/min) and then 10% formaldehyde in 1xPBS (5 ml/min), mouse brains were collected and further incubated overnight at 4°C in 10% formaldehyde and washed three times with 1xPBS for 30 min. The cortices were dissected and used for iDISCO$^+$ clearing as described initially and further updated in https://idisco.info/idisco-protocol/. Briefly, during the iDISCO$^+$ protocol, we stained the tdTomato expressing cells with an anti-RFP antibody (1:1,200 dilution, Rockland, 600-401-379) for 5 days followed by Alexa-647 conjugated donkey anti-rabbit secondary antibody (1:1,000 dilution, Jackson ImmunoResearch, 711-605-152) for 5 days.

Cortex vs striatum quantification: ChAT-CreXAi14 mice were anesthetized with isoflurane as described above and administered an intraperitoneal injection of 200 mg/kg sodium pentobarbital. Following trans-cardiac perfusion with 1xPBS (5 ml/min) and then 10% formaldehyde in 1xPBS (5 ml/min), mouse brains were collected and further incubated overnight at 4°C in 10% formaldehyde and washed three times with 1xPBS for 30 min. Brains were cryopreserved in 30% sucrose/ 1xPBS solution overnight and embedded in OCT.

Light-sheet microscopy

Cortices were subjected to light-sheet microscopy (UltraMicroscope II, LaVision BioTec) operated by the Inspector Pro software (LaVision BioTec) using a fixed objective lens with 2× magnification of 4× 0.3NA. Images were acquired with a Neo sCMOS camera (2,560 × 2,160, pixel size 6.5 μm × 6.5 μm, Andor) in 16 bit. Cortical samples were attached to the sample holder with epoxy glue and placed in a 100% quartz imaging chamber (LaVision BioTec). The light sheet was generated by independent lasers (Module Gen. II, LaVision BioTec); autofluorescence and VChIs were excited by 488 and 639 nm lasers, respectively. All autofluorescence scans were taken at estimated sheets of 10 μm and 4 μm z-step size with no horizontal focusing and signals were detected with Em 525 nm/50 nm filters. VChI scans were taken at an estimated 3.86 μm sheet width and 1 μm z-step size with an 8-steps horizontal focusing. Signals were detected with Em 690 nm/50 nm filters.

Confocal microscopy and immunofluorescence

For quantification of the tdTomato signal and ChAT immunofluorescence (Appendix Fig S7), 3 ChAT-CreXAi14 mice were perfused by trans-cardiac perfusion as described above. Postfixation brains were cryopreserved in 30% sucrose/PBS with sodium azide 0.02% (NaN_3). Brains were sectioned at 30um and subjected to the immunofluorescence protocol using the ChAT antibody (ab144p Merck) at 1:100 concentration. Briefly, sections were washed in PBS, permeabilized with PBS/0.2% Tween-20 for 1 h, and incubated with the primary antibody at 4°C for 72 h in 1xPBS/0.2% Triton-X100, washed five times with 1xPBS/0.2% Triton-X100 and incubated with a secondary antibody (Donkey anti-goat Jackson Immuno-research, 705-605-147) for 2 h at RT. Sections were washed with 1xPBS/0.2% Triton-X100 and mounted with (Thermo Scientific™ Shandon™ Immu-Mount™ - FIS9990402UOM). All confocal images were generated with an Olympus fv-10i scanning confocal ×60 water immersion objective 1.2NA.

Transmission electron microscopy

TEM was performed at the Hebrew University's Nano-Center as follows. Direct imaging of the samples was performed using cryogenic transmission electron microscopy (cryo-TEM). In this method, 3 μl of the solution was deposited on a glow-discharged TEM grid (300 mesh Cu Lacey substrate, Ted Pella, Ltd.). Vitrobot Mark IV (FEI) was used to blot the excess liquid in a controlled environment and to vitrify the specimens by a rapid plunging into liquid ethane pre-cooled with liquid nitrogen. The vitrified samples were examined at −177°C using an FEI Tecnai 12 G2 TWIN TEM operated at 120 kV

Downloaded from https://www.embopress.org on December 26, 2023 from IP 132.64.53.73.

RIGHTSLINK

and equipped with a Gatan 626 cold stage. TIA (Tecnai Imaging & Analysis) software was used to record the images in low dose mode on a 4 K × 4 K FEI Eagle CCD (charge-coupled device) camera. To overcome image internal gradients and noise, we applied a pseudo flat field correction (Fiji, biovoxel) and then local contrast transformation (Fiji, CLAHE) and a smoothing gaussian filter (Sigma – 6px).

PopRec pipeline

Each light-sheet scan was cropped such that only the cortex region was kept, and the barrel cortex region was traced and defined as an ROI (FIJI; Schindelin *et al*, 2012) based on normalized (Intensify3D) autofluorescent scans. Peripheral barrel cells were defined (Fig 4H) by expanding the region volume outward by 20% and ignoring cells in the barrel region. Processed signal scans were normalized across experimental groups with (Intensify3D^{+}) and neuron somata were detected by a Somas to Cubes App. Somata detection coordinates were overlaid on a Z-projected image and accurate detection was determined depending on whether the spot had clear neurites or not (Dataset EV1). A cube was isolated around each neuron, and the data were saved as individual 3D tiff files (MATLAB). Cubes were sized 350 × 500 × 350 pixels (x, y resolution – 0.812pixel/micron, z steps – 1pixel/micron). Samples were oriented before imaging such that the y-axis was perpendicular to the cortical surface. Image cubes were fed to a MATLAB script running on a Linux cluster (see codes on repository). Morphological features from candidate reconstructions were extracted for each cell (Python) and were filtered using a dedicated App – Reconstruction Validation (MATLAB and Vaa3D; Peng *et al*, 2014). Cortical surface and bottom border (Callosum) were measured from autofluorescent scans. All MATLAB and python codes are available as Codes.zip file in the repository.

Morphology features

Accurate definition of features described in this manuscript can be found at: https://neurom.readthedocs.io/en/stable/definitions.html. Additional explanations can be found in Dataset EV2.

Movies

Movies EV1 and EV2 were edited and rendered with IMARIS (Bitplane). Movie EV2 was initially filtered to remove bright noise puncta. Movies EV3 and EV4 were rendered and produced in FIJI.

Statistical analysis of morphological differences and clustering

Statistical analysis was performed with MATLAB (MathWorks). tSNE clustering was performed on 30 standardized (*z*-score, MATLAB) morphological features. To account for known biological variabilities such as repeated measures (animals) or animal sex, we used a linear mixed effects approach as described in https://www.mathworks.com/help/stats/fitlme.html. Detailed models are described in Datasets EV3 and EV4.

Single-nuclei tissue dissociation

To obtain samples for RNA-seq, whisker-deprived and control mice were sacrificed at day 30 by isoflurane anesthesia followed by cervical dislocation. The left and right barrel cortices were dissected and subjected to the NuNeX procedure; tissues were dissected in ice-cold HBSS (Sigma-Aldrich H6648) and immediately transferred to 1 ml of 10% formalin solution (Sigma-Aldrich HT501128) and incubated at RT for 25–30 min. Samples were then washed in 1xPBS, chopped with a scalpel, and homogenized with a Dounce tissue grinder (Sigma-Aldrich, D9063). The homogenate was passed through a 40 μm cell strainer (BD Falcon) and pelleted by centrifugation at 900 *g* for 5 min. Cells were resuspended and stained with DAPI (Santa Cruz) for 10 min. All dissociation and staining steps were performed on ice.

VChI FACS enrichment

To enrich barrel cortex VChIs, we sorted cells based on DAPI and tdTomato signals. We combined cells from several mice to reach roughly 200 VChIs per pool, ensuring that each pool was derived from the same mouse strain, treatment condition, sex, and the same hemisphere. To ensure reproducible experimental conditions, we limited whisker plucking to the right side only. RNA was extracted from the pools of sorted cells with a dedicated kit for formalin-fixed tissues (Qiagen, 217504) according to the manufacturer's instructions. See Dataset EV6 for details on sample characteristics and RIN values. Before cell sorting, NeuN antibody was added for staining (1:500, Alexa Fluor®488 conjugated Sigma MAB377X) and incubated for 30 min. Cells were then pelleted by centrifugation at 900 *g* for 5 min, resuspended in staining buffer, and stained with DAPI (Santa Cruz, DAPI | CAS 28718-90-3) for 10 min. All steps were performed on ice. Cholinergic cells and NeuN-positive/negative cells were sorted through a 70 μm nozzle at a sheath pressure of 70 psi and a drop drive frequency of 90–95 kHz. A highly pure sorting modality (2-way purity sorting) was chosen for both rounds of sorting. The flow rate during the first-round sorting was approximately 5,000 events/s. Sorted cholinergic and DAPI-positive cells were collected into tubes containing 100 μl PKD (< 1,000 cells). The second sort of NeuN-positive/negative from the fixed and fresh tissue cells was sorted into 500 μl staining buffer (> 1,000 cells). Cells sorted from the fixed tissue were centrifuged at 900 *g* for 5 min and resuspended in 100 μl PKD, from the fresh tissue cells were resuspended in 700 μl Qiazol. Samples were collected with BD FACSAria III (BD Biosciences) and analyzed with FCS Express 7 Software (*De Novo* Software).

Library preparation and sequencing

800 pg total RNA from each sample pool was subjected to library construction according to the manufacturer's instructions (SMARTer® Stranded Total RNA-Seq Kit v2 – Pico Input Mammalian, Takara Bio). Libraries were barcoded, pooled, and sequenced with a NextSeq 550 Sequencer (Illumina).

RNA-seq analysis

20 RNA-Seq libraries were subjected to the following analysis pipeline: (i) Adapter trimming with cutadapt (https://cutadapt.readthedocs.io/en/stable/) followed by alignment to the mouse genome (mm10) with STAR (Dobin *et al*, 2013) and detection of differential expressed genes with DESeq2 (Love *et al*, 2014) under R studio (https://rstudio.com/).

Downloaded from https://www.embopress.org on December 26, 2023 from IP 132.64.53.73.

 © 2022 The Authors

PatchSeq RNA-seq analysis

Single nuclei RNA-seq data from the PatchSeq experiment was accessed from the repositories specified in the original study (Gouwens *et al*, 2020). Data were analyzed using python3.9 and Scanpy package (Wolf *et al*, 2018). The initial dataset consisted of 3,840 cells and 45,768 genes. After sorting genes with less than 1,000 total counts, 22,250 genes were left for downstream analysis. Initial data preprocessing included normalization of counts per sample (target sum = 1e4) and log transformation of the normalized counts.

Primary mouse neuron seeding and treatment with siPools

Primary cortical neurons were extracted from PND1-2 mouse pups. Brains were collected in ice-cold 1xHBSS (Sigma H6648), cortices were dissected and meninges removed. Cleaned cortices were dissociated with scissors and enzymatically digested using 60 U Papain (Worthington LS003124) and 15,000 U DNase I (Sigma, DN25), followed by additional digestion using 10,000 U DNase I and thorough trituration. The respective enzymatic reactions were stopped using plating media (MEM-α high-glucose, Biological Industries 01-043-1A, 5% FBS, 1% PS, 1% α-Glu), cells were filtered through a 70 μm cell strainer (BD Falcon) and pelleted at 500 *g* for 5 min. Cells were seeded at a density of 30 k cells/cm^2 either in 0.1 mg/ml poly D-lysine (PDL)-coated 12-well plates (BD Falcon) or on glass coverslips. After 4 h, the media was switched to neurobasal media (Thermo) supplemented with 1% PS, 1% α-Glu, and 2% B27® Supplement (Life Technologies 17504044). SiPools targeting mouse Arpp21, Elmo1, or Sema5b (siTOOLs Biotech GmbH) were added at concentrations 1 and 3 nM together with Lipofectamine RNAiMax (Invitrogen) transfection reagent on day 2; scrambled siPools with no known targets served as negative controls. On day 3 in culture, half of the media was changed and the media was supplemented with Ara-C (Cytosine β-D-arabinofuranoside hydrochloride, Sigma C6645) at a final concentration of 1 μM. RNA for validation of knockdowns was collected on day 4 with TRIZol reagent (Sigma) and stored at −80°C. On day 5, the rest of the neurons were fixed and stained for alpha-tubulin and DAPI according to the protocol below.

Growth and treatment of human neuroblastoma LA-N-2 cell line

The human neuroblastoma cell line LA-N-2 (Sigma-Aldrich: cat. no. 06041202) was grown according to the manufacturer's instructions in MEME/F12, 10% FCS, 1% L-glu, 1% PSA and at 37°C and 5% CO_2. 75,000–100,000 cells /well were grown in 12-well plates.

LA-N-2 cells were seeded 10^5 cells/well in 12-well plates and grown for 24 h or 5 days until transfection with siPools against ELMO1 (1 nM) together with Lipofectamine RNAiMax (Invitrogen) transfection reagent. Following 24 h of transfection, cells were collected for RNA with TRIZol reagent (Sigma), and stored at −80°C, or further fixed and stained for alpha-tubulin and DAPI as explained below.

RNA extraction, cDNA synthesis, and qPCR for primary mouse neurons and LA-N-2 samples

RNA was extracted with miRNeasy Mini Kit (Qiagen, cat. no. 217004) and RNA concentration was measured using Nanodrop; RNA quality was verified using 1%-agarose gel electrophoresis. For cDNA library construction, we used the qScript™ cDNA Synthesis Kit (Qiagen) and qPCR was done using the SYBR Green kit (Qiagen) and with PerfeCTa® SYBR® Green FastMix® (Quanta bio), for each target gene and each sample in triplicates on a BioRad CFX384 real-time PCR cycler. Primer (Sigma-Aldrich) stock solutions of (10 μM) were prepared in RNase-free water and were kept at −20°C. The mouse-specific primers were for Arpp21 (F:GGAGTCAGCAAATAC CACAGACC; R:CTCCTTGCTGACTGCTCATCAC), Elmo1 (F:GCTGT ATTTCGCTAAGCACCACC; R:CTCACACAGCATCTTGGTCAGC), and Sema5b (F:GGCAACTTTGCAGCACGCTTGA; R:AGTGCTCACAC GGTTTCCATGG). Expression was normalized to the housekeeping gene β-actin (F: CCACACCCGCCACCAGTT; R:TACAGCCCGGGGA GCAT).

The human-specific primers included: ChAT (F: TCAT TAATTTCCGCCGTCTC; R: GAGTCCCGGTTGGTGGAGT), SLC18A3 = VAChT (F: CTTGTTATCGTGTGCGTGGC; R: GCGATGTAGTCGGG CACTAT), ELMO1 (F: GGATCCTCATTCCCACTGGC; R: GCAAGA GACCACCCATCACA). Expression was normalized to the housekeeping genes β-actin (ACTB, F: ACAGAGCCTCGCCTTT GCCGA; R: CATGCCCACCATCACGCCCTGG), and ubiquitin C (UBC, F: CAGCCGGGATTTGGGTCG; R: CACGAAGATCTGCATTGT-CAAGT).

Staining and imaging of primary mouse neurons or LA-N-2 cells

Coverslips with cells were washed with PBS, fixed with 2% PFA for 30 min at RT, washed 3xPBS, and then permeabilized with PTx2 solution (0.2% TritonX-100 in PBS). Samples were blocked with 5% NDS in PTx2 for 1 h at RT and then incubated with primary rabbit anti-alpha-tubulin antibody (Abcam, ab18207; 1:200) in 3% NDS and PTwH (0.2% Tween-20 in PBS with 10 μg/mL heparin) overnight at 4°C. Following wash 5× with PTwH, samples were incubated with secondary donkey anti-rabbit Alexa488 (1:500 in 3% NDS in PTwH) for 2 h at RT, washed 3× PTwH, stained with DAPI for 10 min, wash 2× with PTwH and mounted on glass slides and stored at 4°C. Imaging was done with a Wide-field fluorescence microscope - Olympus IX83P2ZF.

Manual Sholl analysis of primary mouse neuron morphology

Primary neuron image labels were hidden from the experimenter. Four circular ROIs for 20, 40, 60, 80 microns were overlaid over the neuron soma and the numbers of intersections were counted manually for each cell (Dataset EV11).

Data availability

All codes used to generate the results are publicly available by a GitHub repository and is where any updates on code and data would be made (https://github.com/nadavyayon/PopRec), RNA-seq files and metadata table are available in ArrayExpress (https://www.ebi.ac.uk/fg/annotare/E-MTAB-12395). The raw and partially processed Light-Sheet images can be found in https://www.ebi.ac.uk/biostudies/bioimages/studies/S-BIAD560. Any additional information or potentially missing information

Downloaded from https://www.embopress.org on December 26, 2023 from IP 132.64.53.73.

RIGHTSLINK

would be happily shared/uploaded to the repository/git upon request.

Expanded View for this article is available online.

Acknowledgements
The authors would like to dedicate this manuscript to the memory of Ms Lili Safra, whose generous support of our Brain center enabled this work and many others. We are also grateful to Dr Sebastian Lobentanzer, Frankfurt, and Shani Vaknine, Jerusalem for advice and assistance in RNA-seq analysis; and to Drs Yoseph Addadi, Rehovot, and Ester R Bennett, David S Greenberg, Sagiv Shifman, Yael Kalisman and Ron Refaeli, Jerusalem for their contributions toward this study. We acknowledge the support of this study by the European Research Council Advanced Award 321501 and the Israel Science Foundation Grant no. 1016/18 (to HS), and a joint Edmond and Lily Safra Center of Brain Sciences (ELSC) grant (to ML and HS) as well as the Gatsby charitable foundation, by the Drahi family foundation (to IS). KW and TZ were supported by postdoctoral ELSC fellowships (KW was a Shimon Peres Fellow at the ELSC), NY, OA, and AD were supported by predoctoral ELSC fellowships, and GA received a summer ELSC fellowship.

Author contributions
Nadav Yayon: Conceptualization; resources; data curation; software; formal analysis; supervision; validation; investigation; visualization; methodology; writing – original draft; project administration; writing – review and editing. **Oren Amsalem:** Conceptualization; resources; software; formal analysis; visualization; methodology; writing – original draft. **Tamara Zorbaz:** Data curation; investigation; visualization; methodology; writing – original draft; writing – review and editing. **Or Yakov:** Data curation; validation; methodology; writing – original draft. **Serafima Dubnov:** Data curation; software; formal analysis; writing – review and editing. **Katarzyna Winek:** Formal analysis; validation; investigation; methodology; writing – review and editing. **Anna K Schmidtner:** Data curation; methodology; writing – review and editing. **Amir Dudai:** Conceptualization; supervision; investigation; visualization. **Gil Adam:** Software; visualization. **Nicolas Renier:** Conceptualization; supervision; methodology; writing – original draft; writing – review and editing. **Marc Tessier-Lavigne:** Conceptualization; supervision; investigation; writing – original draft. **Naomi Habib:** Data curation; supervision; investigation; project administration. **Idan Segev:** Conceptualization; supervision; funding acquisition. **Michael London:** Conceptualization; formal analysis; supervision; investigation; methodology; writing – original draft; project administration; writing – review and editing. **Hermona Soreq:** Conceptualization; resources; supervision; funding acquisition; investigation; visualization; methodology; writing – original draft; project administration; writing – review and editing.

Disclosure and competing interests statement
The authors declare that they have no conflict of interest.

References

Altman RB, Keith Dunker A, Hunter L, Ritchie MD, Murray TA, Klein TE (2016) *Biocomputing 2017: proceedings of the Pacific symposium*. Singapore: World Scientific Publishing Company

Antonopoulos CG, Rubido N, Batista A, Baptista MS (2021) *Advancing our understanding of structure and function in the brain: developing novel approaches for network inference and emergent phenomena*. Lausanne: Frontiers Media SA

Beniaguev D, Segev I, London M (2021) Single cortical neurons as deep artificial neural networks. *Neuron* 109: 2727 – 2739

Blazejczyk M, Macias M, Korostynski M, Firkowska M, Piechota M, Skalecka A, Tempes A, Koscielny A, Urbanska M, Przewlocki R *et al* (2017) Kainic acid induces mTORC1-dependent expression of Elmo1 in hippocampal neurons. *Mol Neurobiol* 54: 2562 – 2578

Chakraborty T, Driscoll MK, Jeffery E, Murphy MM, Roudot P, Chang B-J, Vora S, Wong WM, Nielson CD, Zhang H *et al* (2019) Light-sheet microscopy of cleared tissues with isotropic, subcellular resolution. *Nat Methods* 16: 1109 – 1113

Chen C-C, Tam D, Brumberg JC (2012) Sensory deprivation differentially impacts the dendritic development of pyramidal versus non-pyramidal neurons in layer 6 of mouse barrel cortex. *Brain Struct Funct* 217: 435 – 446

Consonni S, Leone S, Becchetti A, Amadeo A (2009) Developmental and neurochemical features of cholinergic neurons in the murine cerebral cortex. *BMC Neurosci* 10: 18

Coupland CAC, Hill T, Dening T, Morriss R, Moore M, Hippisley-Cox J (2019) Anticholinergic drug exposure and the risk of dementia: a nested case-control study. *JAMA Intern Med* 179: 1084 – 1093

Cuntz H, Forstner F, Borst A, Häusser M (2010) One rule to grow them all: a general theory of neuronal branching and its practical application. *PLoS Comput Biol* 6: e1000877

Cuntz H, Bird AD, Mittag M, Beining M, Schneider M, Mediavilla L, Hoffmann FZ, Deller T, Jedlicka P (2021) A general principle of dendritic constancy: a neuron's size- and shape-invariant excitability. *Neuron* 109: 3647 – 3662

Dobin A, Davis CA, Schlesinger F, Drenkow J, Zaleski C, Jha S, Batut P, Chaisson M, Gingeras TR (2013) STAR: ultrafast universal RNA-seq aligner. *Bioinformatics* 29: 15 – 21

Dudai A, Yayon N, Lerner V, Tasaka G-I, Deitcher Y, Gorfine K, Niederhoffer N, Mizrahi A, Soreq H, London M (2020) Barrel cortex VIP/ChAT interneurons suppress sensory responses *in vivo*. *PLoS Biol* 18: e3000613

Eggermann E, Kremer Y, Crochet S, Petersen CCH (2014) Cholinergic signals in mouse barrel cortex during active whisker sensing. *Cell Rep* 9: 1654 – 1660

von Engelhardt J, Eliava M, Meyer AH, Rozov A, Monyer H (2007) Functional characterization of intrinsic cholinergic interneurons in the cortex. *J Neurosci* 27: 5633 – 5642

Erzurumlu RS, Gaspar P (2012) Development and critical period plasticity of the barrel cortex. *Eur J Neurosci* 35: 1540 – 1553

Eyal G, Mansvelder HD, de Kock CPJ, Segev I (2014) Dendrites impact the encoding capabilities of the axon. *J Neurosci* 34: 8063 – 8071

Farrell MR, Holland FH, Shansky RM, Brenhouse HC (2016) Sex-specific effects of early life stress on social interaction and prefrontal cortex dendritic morphology in young rats. *Behav Brain Res* 310: 119 – 125

Feldman DE, Brecht M (2005) Map plasticity in somatosensory cortex. *Science* 310: 810 – 815

Furney SJ, Simmons A, Breen G, Pedroso I, Lunnon K, Proitsi P, Hodges A, Powell J, Wahlund L-O, Kloszewska I *et al* (2011) Genome-wide association with MRI atrophy measures as a quantitative trait locus for Alzheimer's disease. *Mol Psychiatry* 16: 1130 – 1138

Geula C, Mesulam M-M (1989) Cortical cholinergic fibers in aging and Alzheimer's disease: a morphometric study. *Neuroscience* 33: 469 – 481

Gouwens NW, Sorensen SA, Baftizadeh F, Budzillo A, Lee BR, Jarsky T, Alfiler L, Baker K, Barkan E, Berry K *et al* (2020) Integrated

Downloaded from https://www.embopress.org on December 26, 2023 from IP 132.64.53.73.

 © 2022 The Authors

Morphoelectric and transcriptomic classification of cortical GABAergic cells. *Cell* 183: 935 – 953

Granger AJ, Wang W, Robertson K, El-Rifai M, Zanello AF, Bistrong K, Saunders A, Chow BW, Nuñez V, García MT *et al* (2020) Cortical ChAT neurons co-transmit acetylcholine and GABA in a target- and brain-region-specific manner. *Elife* 9: e57749

Gutierrez H, Davies AM (2011) Regulation of neural process growth, elaboration and structural plasticity by NF-κB. *Trends Neurosci* 34: 316 – 325

Habib N, Li Y, Heidenreich M, Swiech L, Avraham-Davidi I, Trombetta JJ, Hession C, Zhang F, Regev A (2016) Div-seq: single-nucleus RNA-seq reveals dynamics of rare adult newborn neurons. *Science* 353: 925 – 928

Habib N, Avraham-Davidi I, Basu A, Burks T, Shekhar K, Hofree M, Choudhury SR, Aguet F, Gelfand E, Ardlie K *et al* (2017) Massively parallel single-nucleus RNA-seq with DroNc-seq. *Nat Methods* 14: 955 – 958

Horch HW, Krüttgen A, Portbury SD, Katz LC (1999) Destabilization of cortical dendrites and spines by BDNF. *Neuron* 23: 353 – 364

Jung JS, Zhang KD, Wang Z, McMurray M, Tkaczuk A, Ogawa Y, Hertzano R, Coate TM (2019) Semaphorin-5B controls spiral ganglion neuron branch refinement during development. *J Neurosci* 39: 6425 – 6438

Jurgens HA, Amancherla K, Johnson RW (2012) Influenza infection induces neuroinflammation, alters hippocampal neuron morphology, and impairs cognition in adult mice. *J Neurosci* 32: 3958 – 3968

Kasthuri N, Hayworth KJ, Berger DR, Schalek RL, Conchello JA, Knowles-Barley S, Lee D, Vázquez-Reina A, Kaynig V, Jones TR *et al* (2015) Saturated reconstruction of a volume of neocortex. *Cell* 162: 648 – 661

Lendvai B, Stern EA, Chen B, Svoboda K (2000) Experience-dependent plasticity of dendritic spines in the developing rat barrel cortex *in vivo*. *Nature* 404: 876 – 881

Li X, Yu B, Sun Q, Zhang Y, Ren M, Zhang X, Li A, Yuan J, Madisen L, Luo Q *et al* (2018) Generation of a whole-brain atlas for the cholinergic system and mesoscopic projectome analysis of basal forebrain cholinergic neurons. *Proc Natl Acad Sci U S A* 115: 415 – 420

Li Q, Cheng Z, Zhou L, Darmanis S, Neff NF, Okamoto J, Gulati G, Bennett ML, Sun LO, Clarke LE *et al* (2019) Developmental heterogeneity of microglia and brain myeloid cells revealed by deep single-cell RNA sequencing. *Neuron* 101: 207 – 223

Lin S-C, Brown RE, Hussain Shuler MG, Petersen CCH, Kepecs A (2015) Optogenetic dissection of the basal forebrain neuromodulatory control of cortical activation, plasticity, and cognition. *J Neurosci* 35: 13896 – 13903

Liu H-Y, Hong Y-F, Huang C-M, Chen C-Y, Huang T-N, Hsueh Y-P (2013) TLR7 negatively regulates dendrite outgrowth through the Myd88-c-Fos-IL-6 pathway. *J Neurosci* 33: 11479 – 11493

Lobentanzer S, Hanin G, Klein J, Soreq H (2019) Integrative transcriptomics reveals sexually dimorphic control of the cholinergic/neurokine interface in schizophrenia and bipolar disorder. *Cell Rep* 29: 764 – 777

Love MI, Huber W, Anders S (2014) Moderated estimation of fold change and dispersion for RNA-seq data with DESeq2. *Genome Biol* 15: 550

Maravall M, Koh IYY, Lindquist WB, Svoboda K (2004) Experience-dependent changes in basal dendritic branching of layer 2/3 pyramidal neurons during a critical period for developmental plasticity in rat barrel cortex. *Cereb Cortex* 14: 655 – 664

Markram H, Muller E, Ramaswamy S, Reimann MW, Abdellah M, Sanchez CA, Ailamaki A, Alonso-Nanclares L, Antille N, Arsever S *et al* (2015) Reconstruction and simulation of neocortical microcircuitry. *Cell* 163: 456 – 492

Mi H, Ebert D, Muruganujan A, Mills C, Albou L-P, Mushayamaha T, Thomas PD (2021) PANTHER version 16: a revised family classification, tree-based classification tool, enhancer regions and extensive API. *Nucleic Acids Res* 49: D394 – D403

Moolman DL, Vitolo OV, Vonsattel J-PG, Shelanski ML (2004) Dendrite and dendritic spine alterations in Alzheimer models. *J Neurocytol* 33: 377 – 387

Motta A, Berning M, Boergens KM, Staffler B, Beining M, Loomba S, Hennig P, Wissler H, Helmstaedter M (2019) Dense connectomic reconstruction in layer 4 of the somatosensory cortex. *Science* 366: eaay3134

Murakami TC, Mano T, Saikawa S, Horiguchi SA, Shigeta D, Baba K, Sekiya H, Shimizu Y, Tanaka KF, Kiyonari H *et al* (2018) A three-dimensional single-cell-resolution whole-brain atlas using CUBIC-X expansion microscopy and tissue clearing. *Nat Neurosci* 21: 625 – 637

Obermayer J, Luchicchi A, Heistek TS, de Kloet SF, Terra H, Bruinsma B, Mnie-Filali O, Kortleven C, Galakhova AA, Khalil AJ *et al* (2020) Author correction: Prefrontal cortical ChAT-VIP interneurons provide local excitation by cholinergic synaptic transmission and control attention. *Nat Commun* 11: 794

Oh SW, Harris JA, Ng L, Winslow B, Cain N, Mihalas S, Wang Q, Lau C, Kuan L, Henry AM *et al* (2014) A mesoscale connectome of the mouse brain. *Nature* 508: 207 – 214

Peng H, Bria A, Zhou Z, Iannello G, Long F (2014) Extensible visualization and analysis for multidimensional images using Vaa3D. *Nat Protoc* 9: 193 – 208

Peng H, Hawrylycz M, Roskams J, Hill S, Spruston N, Meijering E, Ascoli GA (2015) BigNeuron: large-scale 3D neuron reconstruction from optical microscopy images. *Neuron* 87: 252 – 256

Petersen CCH (2007) The functional organization of the barrel cortex. *Neuron* 56: 339 – 355

Quan T, Zhou H, Li J, Li S, Li A, Li Y, Lv X, Luo Q, Gong H, Zeng S (2016) NeuroGPS-tree: automatic reconstruction of large-scale neuronal populations with dense neurites. *Nat Methods* 13: 51 – 54

Rehfeld F, Maticzka D, Grosser S, Knauff P, Eravci M, Vida I, Backofen R, Wulczyn FG (2018) The RNA-binding protein ARPP21 controls dendritic branching by functionally opposing the miRNA it hosts. *Nat Commun* 9: 1235

Renier N, Wu Z, Simon DJ, Yang J, Ariel P, Tessier-Lavigne M (2014) iDISCO: a simple, rapid method to immunolabel large tissue samples for volume imaging. *Cell* 159: 896 – 910

Renier N, Adams EL, Kirst C, Wu Z, Azevedo R, Kohl J, Autry AE, Kadiri L, Umadevi Venkataraju K, Zhou Y *et al* (2016) Mapping of brain activity by automated volume analysis of immediate early genes. *Cell* 165: 1789 – 1802

Sarna JR, Dyck RH, Whishaw IQ (2000) The Dalila effect: C57BL6 mice barber whiskers by plucking. *Behav Brain Res* 108: 39 – 45

Satoh K, Armstrong DM, Fibiger HC (1983) A comparison of the distribution of central cholinergic neurons as demonstrated by acetylcholinesterase pharmacohistochemistry and choline acetyltransferase immunohistochemistry. *Brain Res Bull* 11: 693 – 720

Saunders A, Granger AJ, Sabatini BL (2015) Corelease of acetylcholine and GABA from cholinergic forebrain neurons. *Elife* 4: e06412

Schindelin J, Arganda-Carreras I, Frise E, Kaynig V, Longair M, Pietzsch T, Preibisch S, Rueden C, Saalfeld S, Schmid B *et al* (2012) Fiji: an open-source platform for biological-image analysis. *Nat Methods* 9: 676 – 682

Sholl DA (1953) Dendritic organization in the neurons of the visual and motor cortices of the cat. *J Anat* 87: 387 – 406

Downloaded from https://www.embopress.org on December 26, 2023 from IP 132.64.53.73.

RIGHTSLINK

Susaki EA, Tainaka K, Perrin D, Kishino F, Tawara T, Watanabe TM, Yokoyama C, Onoe H, Eguchi M, Yamaguchi S *et al* (2014) Whole-brain imaging with single-cell resolution using chemical cocktails and computational analysis. *Cell* 157: 726 – 739

Tomer R, Ye L, Hsueh B, Deisseroth K (2014) Advanced CLARITY for rapid and high-resolution imaging of intact tissues. *Nat Protoc* 9: 1682 – 1697

de la Torre-Ubieta L, Bonni A (2011) Transcriptional regulation of neuronal polarity and morphogenesis in the mammalian brain. *Neuron* 72: 22 – 40

Wolf FA, Angerer P, Theis FJ (2018) SCANPY: large-scale single-cell gene expression data analysis. *Genome Biol* 19: 15

Yayon N, Dudai A, Vrieler N, Amsalem O, London M, Soreq H (2018) Intensify3D: normalizing signal intensity in large heterogenic image stacks. *Sci Rep* 8: 4311

License: This is an open access article under the terms of the Creative Commons Attribution-NonCommercial-NoDerivs License, which permits use and distribution in any medium, provided the original work is properly cited, the use is non-commercial and no modifications or adaptations are made.

Downloaded from https://www.embopress.org on December 26, 2023 from IP 132.64.53.73.

 © 2022 The Authors